Unveiling Mesoscopic Structures in Distorted Lamellar Phases through Deep Learning-Based Small Angle Scattering Analysis

Chi-Huan Tung[a], Yu-Jung Hsiao[a], Hsin-Lung Chen[a], Guan-Rong Huang[b], Lionel Porcar[c], Ming-Ching Chang[d], Jan-Michael Carrillo[e], Yangyang Wang[e], Bobby G. Sumpter[e], Yuya Shinohara[f], Jon Taylor[g], Changwoo Do[g], Wei-Ren Chen[g]

[a]*Department of Chemical Engineering, National Tsing Hua University, Hsinchu, 30013, Taiwan*
[b]*Department of Materials and Optoelectronic Science, National Sun Yat-sen University, Kaohsiung, 80424, Taiwan*
[c]*Institut Laue-Langevin, B.P. 156, F-38042 Grenoble Cedex 9, France*
[d]*Department of Computer Science, University at Albany - State University of New York, Albany, 12222, New York, United States*
[e]*Center for Nanophase Materials Sciences, Oak Ridge National Laboratory, Oak Ridge, 37831, Tennessee, United States*
[f]*Materials Science and Technology Division, Oak Ridge National Laboratory, Oak Ridge, 37831, Tennessee, United States*
[g]*Neutron Scattering Division, Oak Ridge National Laboratory, Oak Ridge, 37831, Tennessee, United States*

Abstract

Hypothesis

The morphology of a lamellar phase, which is mainly characterized by stacked parallel layers, is often accompanied by interconnected network structures which is a feature of bicontinuous sponge phase. However, conventional scattering function based on deterministic modeling cannot express such structural features in full extend. , face a significant challenge in analytically expressing scattering functions with relevant structural parameters. We hypothesize that a stochastic deep learning approach can quantitatively reveal the inherent correlations within these phases.

Experiments and Simulations

This report outlines a novel strategy that integrates convolutional neural networks, supported by stochastically generated density fluctuations, into the regression analysis framework for addressing the persistent challenge of structural inversion in lyotropic phases using scattering data. To evaluate the efficacy of our proposed approach, we conducted computational accuracy assessments and applied it to the analysis of experimentally measured small-angle neutron scattering cross-sections of a commonly studied lamellar phase.

Findings

The findings unambiguously demonstrate that deep learning provides a dependable and quantitative approach to investigating the morphology of diverse lyotropic phases. It is adaptable for application to lamellar, sponge, and intermediate structures exhibiting fused topological features, offering a unified structural characterization of lyotropic systems. In essence, this study underscores the capability of deep learning techniques in addressing intricate challenges within the realm of soft matter structures and beyond.

Keywords: Lamellar Phases, Small Angle Scattering, Deep Learning, Generalized Levelled Wave

---

1. Introduction

Amphiphilic molecules have a fascinating ability to undergo self-organization when dissolved in a solution, giving rise to the formation of two-dimensional bilayers. They exhibit intricate and intriguing structures when examined at a mesoscopic scale, a phenomenon that falls under the category of lyotropic phases. Mesoscopic morphology plays a central role in lyotropic systems, influencing a wide range of natural and synthetic processes, from the formation of cell membranes to the development of novel materials with unique characteristics [1, 2].

Among the various lyotropic phases, the swollen lamellar phase, often represented as L_α, stands out due to its remarkably well-organized parallel planes. Considerable effort has been directed towards characterizing its unique nonparticulate structures. Small angle scattering of neutrons and X-rays is a crucial method employed for this purpose [3, 4]. In the context of these experiments, it becomes necessary to derive an analytical expression for the coherent scattering of L_α phases in reciprocal space, denoted by the variable Q, based on relevant parameters. The morphology of these phases is then unveiled through the refined parameters obtained via a regression analysis of the collected spectra.

For L_α phases, a widely adopted scattering function model was introduced by Nallet, Laversanne, and Roux, which conceptualizes the system as a stake of parallel lamellar plates [5]. Within this framework, the coherent scattering cross sections can be conveniently decomposed into the product of two components: the inter-planar structure factor $S(Q)$, which represents the average displacement between these planes and its distribution, and the form factor $P(Q)$, which characterizes the density fluctuations within each plane. The validity of this ideal one-dimensional ordered lamellar structures premises on the preservation of long-range translational order of density fluctuation of parallel planes [6]. To account for any localized deviations in the lamellar surfaces, numerous scattering functions have been devised by incorporating expressions of $P(Q)$. These functions are designed to explore the intricate aspects of diffuse scattering that can be observed in various L_α phases [7–13].

However, supported by prior Nuclear Magnetic Resonance (NMR) investigations [14–17], it has been long recognized that a substantial portion of lamellar phases exhibits imperfect structural attributes. These imperfections, specifically characterized as passages or perforations within adjacent plates

[4, 18–20], disrupt the uniform alignment of the in-plane normal vector—an inherent characteristic of the ideal L_α phase. As a result, the long-range order within these phases no longer exhibits infinite correlation.

Nonetheless, due to the enduring remnants of lamellar organization, the orientational distribution of the normal vector maintains a degree of non-random lamellar order, distinguishing it from the intrinsic randomness observed in L_3 states, a sponge phase notable for its distinctive isotropic structure arising from the intricate interconnection of bilayers. The quantitative analysis of the structure within this distorted lamellar phase presents a significant and formidable challenge [21]. This challenge encompasses two essential dimensions: first, it demands the precise identification of parameters capable of accurately characterizing the topological features of distorted L_α phases with limited long-range order; and second, it calls for the development of an analytical expression for the corresponding scattering function, which serves as the foundational cornerstone for spectral inversion analysis. It is this challenge that serves as the driving impetus behind the ongoing research endeavor.

In the context of inverting the topological characteristics of distorted lamellar phases obtained from scattering data, our standpoint is that conventional deterministic methods may not necessarily provide the most advantageous solution. This constraint predominantly arises from the anticipated complexity involved in accurately delineating the highly nonlinear bijective relationship between the topological properties of imperfect lamellar phases, encompassing both the L_3 and L_α structures, and the two-point correlation function. In this scholarly report, we present a deep learning approach as a method to address these mathematical challenges.

In this research, our initial step involves the regulation of the random distribution of wave vectors within the leveled wave model as introduced by Berk [22, 23]. This regulation aims to characterize density fluctuations within the L_3 phases. Through this process, we are able to identify a specific set of parameters that effectively describe the topological attributes of distorted structures within the L_α phase. Subsequently, we create an extensive repository of two-point correlation functions, which are generated using the identified parameter settings that closely mimic real experimental systems exhibiting the L_α phase. This repository serves as the training dataset for establishing a probabilistic connection between the topological parameters and coherent scattering functions. To achieve this, we employ a conventional neural network (CNN), which is trained through a series of linear matrix op-

erations, facilitating this crucial link. To assess the computational accuracy of the CNN-based regression algorithm, we also generate an additional comprehensive repository of two-point correlation functions. This second set is created using a distinct set of topological parameters that were not originally included in the training dataset. The purpose of this is to benchmark the performance of the algorithm through numerical evaluations.

Our study confirms the feasibility of using this deep learning approach for structural analysis through experimentation. Specifically, we apply this approach to small-angle neutron scattering (SANS) on a lyotropic system composed of stacked lamellar plates with varying degrees of fragmentation. In the following section, we delve into a more detailed exposition of the development of our methodology.

2. Methods

This section introduces the Generalized Levelled Wave (GLW) approach as the descriptive framework for characterizing the mesoscopic structures within general lyotropic phases, along with applying the Convolutional Neural Network (CNN) as the foundation for regression analysis of scattering measurements.

2.1. Generalized Levelled Wave (GLW) Method

It is instructive to present the levelled wave method as originally conceived by Berk [22, 23]. This method characterizes the density fluctuations in bicontinuous systems within real space $\mathbf{r}$ using the following expression:

$$S(\mathbf{r}) = \frac{1}{\sqrt{N\langle A^2\rangle}} \sum_{n=1}^{N} A_n \cos(k\hat{\mathbf{k}}_n \cdot \mathbf{r} + \phi_n), \tag{1}$$

In Eqn. (1), the unit random wave vectors denoted as $\hat{\mathbf{k}}$ are uniformly distributed across the entire solid angle of 4π. The magnitude k follows a normal distribution with specified mean and variance. The phase angles ϕ_n are evenly distributed over the interval of 2π. Each partial wave indexed by n is associated with a coefficient A_n. The entire set of N plane waves is standardized by dividing by the variance of these coefficients, which is $\frac{1}{\sqrt{N\langle A^2\rangle}}$. Consequently, the quantity $S(\mathbf{r})$ can be considered an ensemble of random variables with a mean of 0 and a variance of 1.

A threshold value denoted as α is introduced and applied to the normally distributed $S(\mathbf{r})$ to demarcate the two coexisting phases within the bicontinuous structure. Within a two-phase system, the parameter α is closely linked to the ratio of the volume fractions of the two coexisting phases. To enhance the scattering contrast, two distinct scattering length densities (SLD) can be assigned to these phases. With the parameter α in place, Equation (1) can be further subjected to Fourier transformation to generate the scattering amplitude $F(Q)$ in reciprocal Q space. The coherent small angle scattering profile $I(Q)$ can be readily obtained by squaring $F(Q)$. In this specific context, scattering functions with relevant parameters have been developed to extract the topological characteristics of the bicontinuous L_3 phase from experimentally acquired coherent small-angle scattering data, as documented in references such as [3, 24–26].

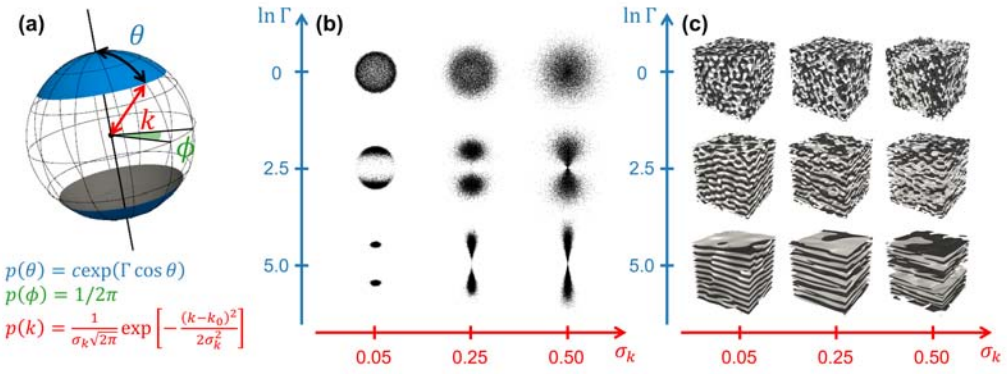

Figure 1: (a) Visual representation of the definition of anisotropic wave vector distribution within spherical coordinates, underpinning the GLW approach. (b) The dependence of wave vector distribution on the orientational order parameter in the polar angle direction (Γ) and the radial dispersion parameter (σ_k). (c) The corresponding three-dimensional lyotropic structures in real $\mathbf{r}$ space which are three-dimensional lyotropic structures in real space that are statistically equivalent to the wave vector distribution given in (b) through the principle of ensemble average.

When the topological characteristics of lyotropic systems deviate from the sponge conformation, the normal vector fields of the interface between the two interpenetrating phases can no longer be represented by the randomly oriented $\hat{\mathbf{k}}$. To address the increasing lamellar order, an additional constraint on the orientational order $\hat{\mathbf{k}}$ proposed in [22, 23] is imposed according to the schematic representation given in Fig. 1(a): The polar component distribu-

tion of $\hat{\mathbf{k}}$ is no longer characterized by random distribution over a 4π sphere. Instead, following Fisher's recommendation [27], the distribution function along the polar angle θ direction is expressed as follows

$$P(\theta) = c \exp(\Gamma \cos\theta), \tag{2}$$

Here, c represents a constant, and Γ denotes the orientational order parameter used to quantify the directional dispersion of $\hat{\mathbf{k}}$ along the direction of θ.

Furthermore, in the case of general lyotropic systems exhibiting lamellar order, as there is no compelling rationale to suggest the presence of any preferred direction for in-plane density fluctuations at the interface, the distribution of $\hat{\mathbf{k}}$ along the azimuthal angle ϕ is modeled by a uniform distribution, as expressed below:

$$P(\phi) = \frac{1}{2\pi}, \tag{3}$$

The distribution of $\hat{\mathbf{k}}$ along the radial direction remains unchanged, in accordance with the initial definition of the normal distribution proposed by Berk [22, 23]. Namely,

$$P(k) = \frac{1}{\sigma_k \sqrt{2\pi}} \exp[-\frac{(k-k_0)^2}{\sigma_k^2}], \tag{4}$$

where k_0 is the mean and σ_k denotes the standard deviation characterizing the radial dispersion of k given in Eqn. (1).

In this representation, referred to as the Levelled Wave (GLW) method, the relationship between the anisotropic wave vector distribution and the parameters σ_k and Γ is visually depicted in Fig. 1(b). When σ_k is held constant, augmenting the value of Γ engenders a discernibly heightened polarization within the distribution of $\hat{\mathbf{k}}$, resulting in the vectors aligning more closely with the normal axis of the lamellar plates. Conversely, when Γ remains fixed and σ_k is increased, the result is a progressively more diffused distribution in $\hat{\mathbf{k}}$. The corresponding three-dimensional renderings of interfacial conformation are given in Fig. 1(c). As Γ increases, the characteristic anisotropic orientational order of lamellar phases becomes more prominent. Conversely, an increase in σ_k leads to a greater variation in the inter-plane distance across all lyotropic phases.

It is essential to emphasize that within the descriptive framework of GLW, a given lyotropic structure can be defined by three key parameters: σ_k, Γ,

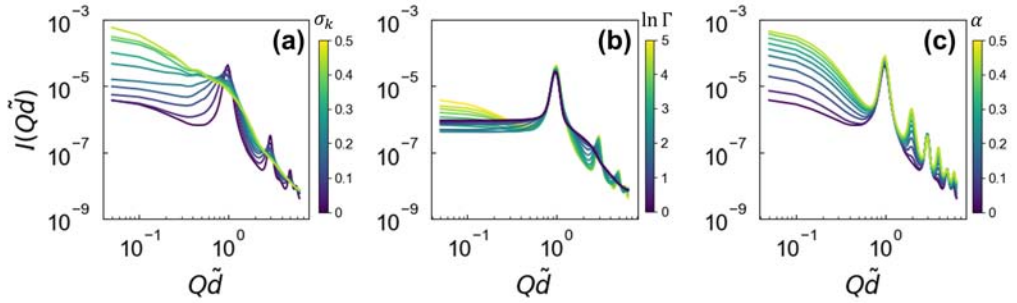

Figure 2: The evolution of $I(Q\tilde{d})$ as a function of (a) σ_k, (b) $\ln\Gamma$, and (c) α. The continuous color scales indicate the probed ranges of each parameter. $\tilde{d}$ represents the average inter-plane distance.

and α. Here a specific set of σ_k, Γ, and α is defined as Ξ. The responsive characteristics of small-angle scattering in lyotropic phases in relation to these parameters are illustrated in Fig. 2. Here the coherent scattering intensity is represented in a dimensionless unit of $Q\tilde{d}$, where $\tilde{d} \equiv \frac{1}{k_0}$ represents the average inter-plane distance of well-ordered lamella. Within the probed ranges, as σ_k increases, all distinctive lamellar peaks in the plot of $I(Q\tilde{d})$ gradually broaden and eventually fade away, as illustrated in Panel (a). Moreover, as shown in Panel (b), when $\ln\Gamma$ increases from 0 to 5, there is a distinct transformation in the behavior of $I(Q\tilde{d})$ transitioning from an expression of an L_3 sponge state to that of an L_α lamellar state. In Panel (c), it becomes clear that adjusting α from 0.5 to 0 gives rise to an intriguing observation: the magnitudes of the even-numbered peaks in $I(Q\tilde{d})$ for the L_α lamellar state gradually diminish and eventually vanish, whereas the odd-numbered peaks remain largely unchanged. Given that α is used to define the interface between two interpenetrating phases within the framework of GLW, it is possible to modify the α value in SANS experiments for a lamellar system by adjusting the difference in scattering length density between surfactant and solvent. As a result, this adjustment results in a unique observation similar to what's shown in Fig. 2(c), as described in a SANS experiment where the contrast was varied in a lamellar phase [28].

2.2. Demonstrating the One-to-one Correspondence: $\Xi \leftrightarrow I(Q\tilde{d})$

It is crucial to assess whether there exists a one-to-one mapping between Ξ and $I(Q\tilde{d})$, a prerequisite for any feasible structural inversion analysis. To conduct this evaluation, we generated 3000 sets of $I(Q\tilde{d})$, denoted as

$\{I_{train}(Q\tilde{d})\}$, using the GLW framework, with Ξ values falling within the ranges illustrated in Fig. 2. Each $I(Q\tilde{d})$ comprises 128 sampled Q points.

To visualize the effect of Ξ on the 128-dimensional $I(Q\tilde{d})$ dataset, we performed a Principal Component Analysis (PCA) employing Singular Value Decomposition (SVD) techniques [29]. The results revealed that the first three singular vectors effectively capture the primary sources of variance within the original data. This suggests that the vector space $\mathbb{R}^3$ defined by these three singular vectors, which we refer to as SVD0, SVD1, and SVD2 in Fig. 3(a), sufficiently express the fundamental features of the interrelated data.

In the three-dimensional vector space defined by the basis vectors SVD0, SVD1, and SVD2, each instance of the expression $I(Q\tilde{d})$ corresponds to a distinct point. As illustrated in Fig. 3, the distribution of this data exhibits a complex, twisted three-dimensional structure. Findings depicted in Panels (b)-(d) of Fig. 3 indicate a smooth variation in the distributions of these parameters. This suggests that the data points are non-overlapping and exhibit significant correlations over a specific length scale. A comprehensive analysis of the data distribution has revealed the absence of any inseparable overlaps, thus confirming a one-to-one mapping between $I(Q\tilde{d})$ and Ξ. This supports the feasibility of inversely deducing these parameters for general lyotropic phases from their experimentally measured scattering cross-sections.

The color scale transformations displayed in Panels (b) through (d) of Fig. 3 demonstrate the linear independence of the gradient vectors associated with these three parameters. In conjunction with the observed assessments of $I(Q\tilde{d})$ in response to variations in σ_k and $\ln\Gamma$, as detailed in Panels (a) and (b) of Fig. 2, it is mathematically unviable to capture the nuanced characteristics of $I(Q\tilde{d})$ through the conventional approach of modifying the 1-D scattering function typically employed for lamellar phases when dealing with general lyotropic phases composed of partially interconnected or incompletely laterally separated membranes, as delineated in [5]. A mere adjustment of $P(Q)$ while considering intra-plate density fluctuations falls short in addressing the features of intricate diffusive scattering in $I(Q\tilde{d})$.

2.3. Development of Regression Algorithm based on Convolutional Neural Network (CNN)

Based on the intricate array of color scales depicted in Fig. 3, the position we take in this study is that the mathematical derivation of an analytical expression for $I(Q\tilde{d})$ as a function of Ξ, represented by the parameters

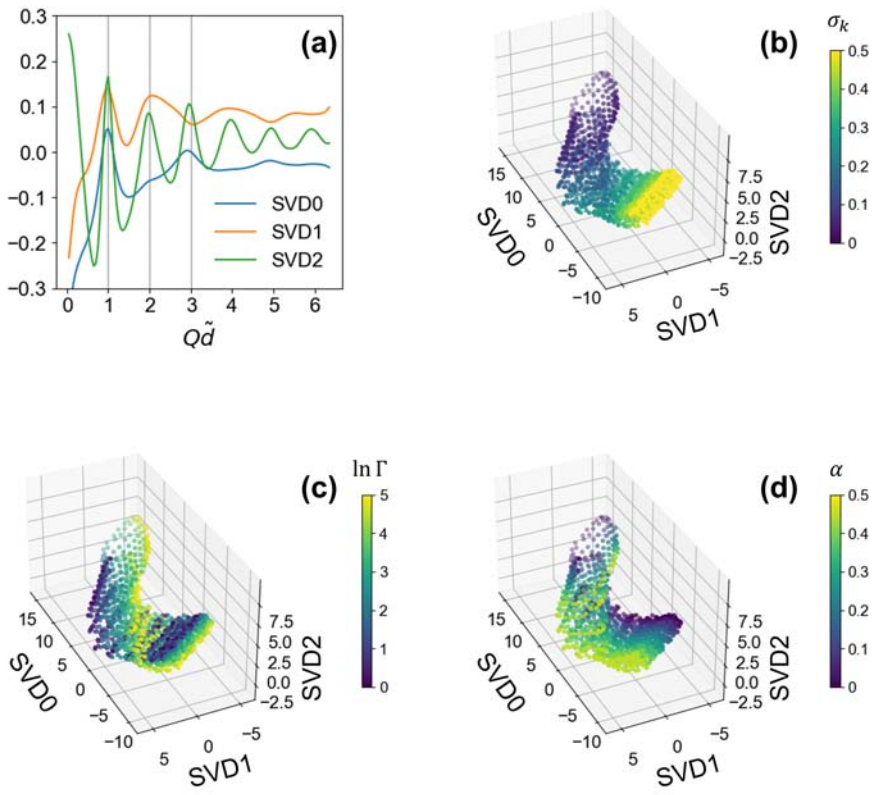

Figure 3: (a) The first three singular vectors SVD0, SVD1, and SVD2 derived through Principal Component Analysis (PCA) of $\{I_{train}(Q\tilde{d})\}$. Panels (b) to (d) illustrate the distributions of σ_k, $\ln\Gamma$, and α within the $\mathbb{R}^3$ vector space defined by SVD0, SVD1, and SVD2 in the manifold of $\{I_{train}(Q\tilde{d})\}$.

$\{\sigma_k, \ln\Gamma, \alpha\}$, is no longer feasible for the broad category of lyotropic systems. Hence, rather than pursuing the deterministic derivation of analytical scattering functions for the precise extraction of structural parameters from the associated scattering cross-sections, a methodology distinct from the prior investigations of L_3 [24, 25] and L_α phases [5] is presented in this report. This novel approach employs a regression framework founded on the principles of deep learning, specifically utilizing a Convolutional Neural Network (CNN), to probabilistically infer Ξ from the observed $I(Q\tilde{d})$.

Fig. 4 illustrates the CNN architecture, which plays a central role in our regression analysis. The CNN comprises two primary components: the

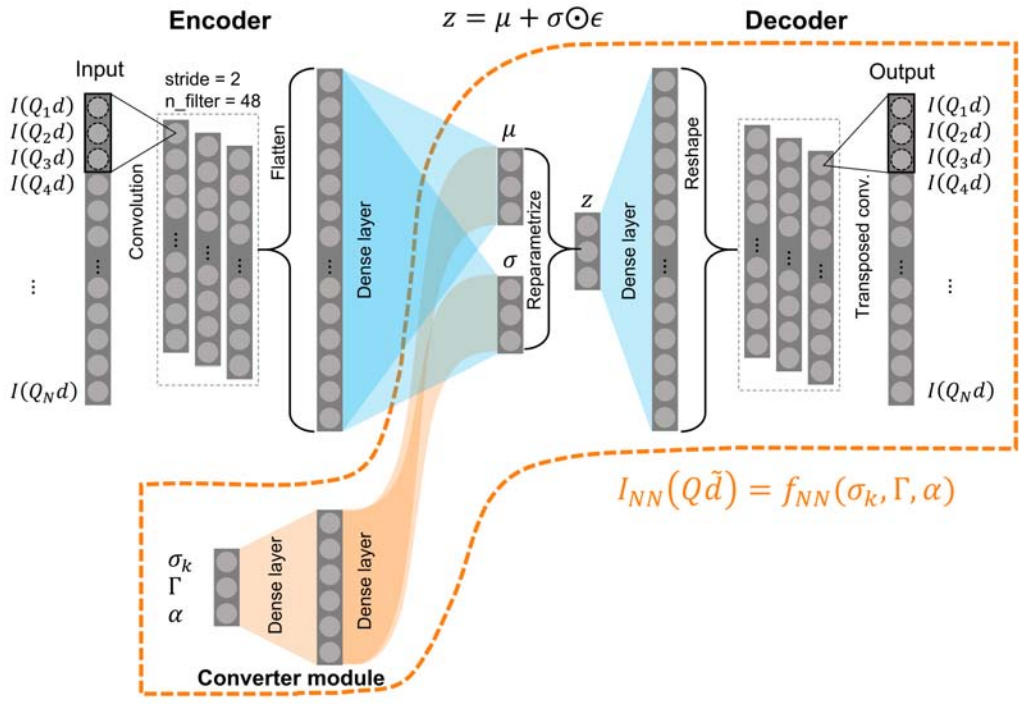

Figure 4: The convolutional neural network (CNN) architecture which constitutes the fundamental framework of regression analysis for inversely inferring $\Xi \equiv \{\sigma_k, \ln\Gamma, \alpha\}$ of lyotropic phases from experimentally measured $I(Q\tilde{d})$.

encoder and the decoder. At the forefront of the encoder lies a convolutional layer, tasked with processing an input denoted as $I_{\text{input}}(Q\tilde{d})$ containing 128 elements. It employs 48 three-element filters to extract the salient features from the input $I(Q\tilde{d})$. As implied by its title, this process is accomplished through the convolution of $I_{\text{input}}(Q\tilde{d})$ with filters. During this operation, a dot product is computed as the filter shifts with a stride of 2. In the end, 48 one-dimensional arrays, each consisting of 64 elements, are generated, collectively known as the feature map. These 48 arrays are subsequently collapsed into one dimension, a step referred to as flattening, to produce a one-dimensional array comprising 3072 elements, which serves as the input for the dense layer located at the back end of the encoder.

The primary function of a dense layer is to consider the effect of each element within the feature map on its output through linear mapping matrix operations, enabling either a reduction or an increase in dimensionality. In

this context, two three-element arrays, denoted as μ and σ, are generated. These arrays are used to generate a random variable, denoted as z, with μ serving as the mean and σ as the standard deviation. This process is designed to mitigate the minor uncorrelated data fluctuations inherent in $I_{\text{input}}(Q\tilde{d})$.

Here, we define $z \equiv \mu + \sigma \odot \epsilon$ as the sum of μ and the element-wise product of σ and ϵ. The symbol $\odot$ represents the element-wise production operator. Then, z serves as an input for the decoder, which possesses the network architecture mirroring that of the encoder. We generate 100 different z values based on 100 unique ϵ values, randomly sampled from a standard normal distribution with a mean of zero and a variance of 1. Consequently, the corresponding 100 different $I(Q\tilde{d})$ outputs are produced. To obtain $I_{\text{output}}(Q\tilde{d})$, we compute an ensemble average of these output values across all ϵ samples. Accordingly, we define a loss function L as $L \equiv \|\ln I_{\text{input}}(Q\tilde{d}) - \ln I_{\text{output}}(Q\tilde{d})\|^2$. We aim to minimize the squared difference in a logarithmic scale because the coherent scattering intensity in typical lyotropic systems often spans several orders of magnitude.

Algorithm 1: Training VAE as a basis of generative model

Input: $I(Q\tilde{d})$
Result: Optimal w^{VAE} for f_{decoder}

$w^{\text{VAE}} \leftarrow w_0^{\text{VAE}}$; `// initialize VAE parameters`
$\mu, \sigma \leftarrow f_{\text{encoder}}(I(Q\tilde{d}))$; `// convert` $I(Q\tilde{d})$ `to the mean and standard deviation of` z
$i \leftarrow 0$
while $i <$ Maxiter **do**
  Generate 100 samples $\epsilon \sim \mathcal{N}(0, 1)$
  $I_{\text{VAE}}(Q\tilde{d}) \leftarrow \langle f_{\text{decoder}}(\mu, \sigma, \epsilon) \rangle_\epsilon$; `// generate` $I(Q)$ `from the ensembe average of the decoder output`
  $L_{\text{VAE}} \leftarrow \left\| I_{\text{VAE}}(Q\tilde{d}) - I(Q\tilde{d}) \right\|^2$; `// evaluate loss function`
  Update w^{VAE} with `Adam` optimizer to minimize L_{VAE}
  $i \leftarrow i + 1$
end

In every training iteration, the values of ϵ remain constant as we compute the backpropagated partial derivatives of L with respect to the network parameters using the chain rule. Subsequently, we adjust the network based

Algorithm 2: Training the $I(Q\tilde{d})$ generator

Input: Ξ, $I(Q\tilde{d})$, pretrained w^{VAE} for f_{decoder}
Result: Optimal w and w^{VAE} such that $I_{\mathrm{NN}}(Q) = f_{\mathrm{NN}}(Q, \Xi)$

Freeze w^{VAE}
$w \leftarrow w_0$; `// initialize converter module`
$i \leftarrow 0$
while $i <$ Maxiter **do**
  Generate 100 samples $\epsilon \sim \mathcal{N}(0, 1)$
  $\mu, \sigma \leftarrow f(\Xi, w)$; `// convert` Ξ `to the mean and standatd deviation of` z
  $I_{\mathrm{NN}}(Q\tilde{d}) \leftarrow \langle f_{\mathrm{decoder}}(\mu, \sigma, \epsilon)\rangle_{\epsilon}$; `// generate` $I(Q)$ `from the ensembe average of the decoder output`
  $L \leftarrow \left\| I_{\mathrm{NN}}(Q\tilde{d}) - I(Q\tilde{d}) \right\|^2$; `// evaluate loss function`
  Update w with `Adam` optimizer to minimize L
  $i \leftarrow i + 1$
end
Unfreeze w^{VAE}
$i \leftarrow 0$
while $i <$ Maxiter **do**
  Generate 100 samples $\epsilon \sim \mathcal{N}(0, 1)$
  $\mu, \sigma \leftarrow f(\Xi, w)$
  $I_{\mathrm{NN}}(Q\tilde{d}) \leftarrow \langle f_{\mathrm{decoder}}(\mu, \sigma, \epsilon)\rangle_{\epsilon}$; `// generate` $I(Q)$ `from the ensembe average of the decoder output`
  $L \leftarrow \left\| I_{\mathrm{NN}}(Q\tilde{d}) - I(Q\tilde{d}) \right\|^2$; `// evaluate loss function`
  $L' \leftarrow L + \alpha \left\| w^{\mathrm{VAE}} \right\|^2$; `// regularization`
  Update w, w^{VAE} with `Adam` optimizer to minimize L'
  $i \leftarrow i + 1$
end
$f_{\mathrm{NN}}(\Xi) \equiv f_{\mathrm{decoder}}(f(\Xi, w), w^{\mathrm{VAE}})$

on these derivatives. Evidently, the primary objective of the training process is to minimize the disparity between the input function $I_{\mathrm{input}}(Q\tilde{d})$ and the output function $I_{\mathrm{output}}(Q\tilde{d})$. The training processes for this generative model

are summarized in Algorithm 1.

In typical regression analyses of scattering experiments, the inputs usually consist of pre-selected structural parameters, as opposed to a one-dimensional array representing the scattering function. Hence, a converter module is designed, comprising two dense layers, to transform the parameters σ_k, $\ln\Gamma$, and α, which are represented as a three-element array, into the corresponding latent variable z. Following further fine-tuning, we introduce an augmented decoder network, denoted by the orange dashed line in Figure 4, designed to facilitate the regression analysis of scattering experiments for general lyotropic phases. We outline the additional training procedure of the $I(Q\tilde{d})$ generator in Algorithm 2.

In essence, the primary objective of employing this deep learning-driven regression analysis is to capture the intricate and inherently nonlinear connection between Ξ and $I(Q\tilde{d})$. This intricate relationship defies conventional analytical methods, necessitating the use of a series of linear operations derived from a dataset $I_{\text{train}}(Q\tilde{d})$ gathered within the parameter space defined by the GLW descriptive framework. To sum up the training process, this approach seeks to model this complex relationship effectively.

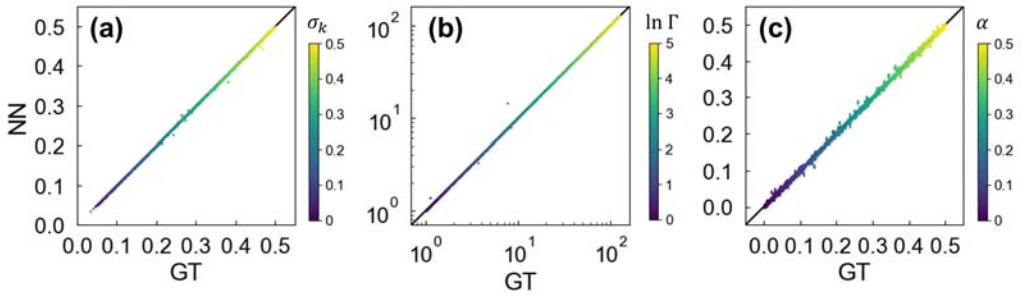

Figure 5: Comparative analysis of parameters inverted by CNN (NN) and the corresponding Ground Truth (GT): (a) σ_k, (b) $\ln\Gamma$, and (c) α were inverted using the CNN regression algorithm (NN) and compared with the ground truth data (GT) represented on the y-axis and x-axis, respectively. The majority of predicted parameters are seen to show quantitative agreement with the GT values.

We generated an additional comprehensive set of $I(Q\tilde{d})$ data, denoted as $I_{\text{test}}(Q\tilde{d})$, using an extensive set of Ξ. This set of data was calculated separately and was not utilized during the training phase. The purpose was to assess the numerical accuracy of the deep learning-based regression algorithm presented in Fig. 4. In Fig. 5, we present a comparison between

the input parameters used in simulations and those obtained through inversion from $I_{\text{test}}(Q\tilde{d})$. Remarkably, all three inverted parameters, referred to as NN, exhibit a high degree of agreement with their computational inputs, referred to as the ground truth (GT). The majority of the inverted parameters closely align with the corresponding ground truths, underscoring the numerical accuracy of this CNN-based regression algorithm. it's worth noting that the statistical uncertainties associated with the inverted α are visibly higher when compared to the other two inverted parameters. This observation suggests that $I(Q\tilde{d})$ is less influenced by changes in α.

3. SANS Experimental Results and Discussion

To demonstrate the feasibility of our proposed deep learning inversion method, we carried out small angle neutron scattering (SANS) of a frequently investigated lyotropic system: Sodium dioctyl sulfosuccinate, commonly referred to as AOT, was commercially available from Thermo Scientific. To produce aqueous AOT solutions with different weight concentrations of 30%, 40%, and 50%, AOT powders were dissolved in deuterium oxide (D_2O) acquired from Sigma Aldrich with a deuteration degree of no less than 99.96 %. These blends were continuously agitated under standard environmental conditions for approximately 4 hours, ultimately yielding optically transparent solutions. It should be noted that the concentration range examined in this study has been previously identified as the equilibrium lamellar phases [30, 31]. The SANS experiment was conducted at the D22 large dynamic range small-angle diffractometer located at the Institut Laue-Langevin (ILL). In this study, we used two wavelengths, 6 Å and 11.5 Å, to cover the essential range of Q from 0.001 Å^{-1} to 0.5 Å^{-1}, where coherent neutron scattering was detected. The AOT aqueous solutions were placed in Hellma banjo cells with a 1 mm pathlength.

Fig. 6 (a) shows the SANS intensity, $I(Q)$, for aqueous solutions containing 30%, 40%, and 50% AOT. Before delving into the quantitative data analysis, it is instructive to explore the qualitative characteristics of $I(Q)$: Upon initial observation, it is evident that with an increase in the weight fraction of AOT, the height of the first correlation peak in $I(Q)$ steadily diminishes, and its position progressively shifts towards higher values of Q. Furthermore, while the states chosen for the SANS study are well situated within the lamellar phases, as indicated by the AOT/water phase diagram [30, 31], the distinctions in lamellar structural organization can be readily

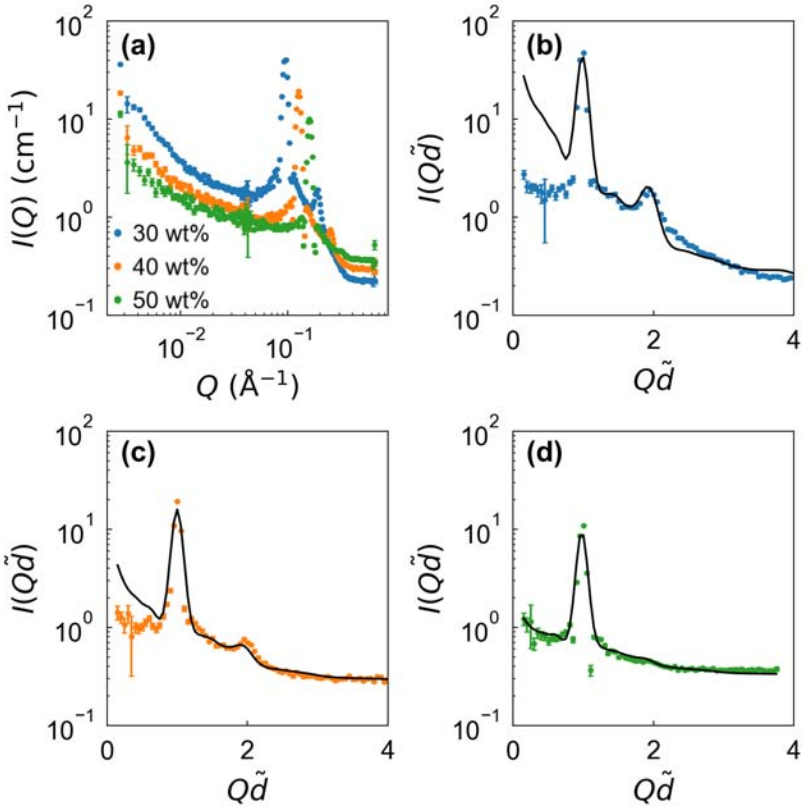

Figure 6: (a) SANS $I(Q)$ for aqueous AOT solutions at three weight fractions of 30% (blue circles) 40% (orange circles) and 50% (green circles). (b) to (d): Comparison between experimental $I(Q)$ (colored symbols) and fitting curves (black lines). The measured $I(Q)$ were desmeared according to [32]

observed through the distinct features in the development of $I(Q)$, including the height and width of the second correlation peak. When the weight fraction of AOT is raised, the incoherent background becomes more prominent due to the higher concentration of protons in the sample.

Figs. 6 (b)-(d) display the comparison between the measured $I(Q)$ and the results of regression analysis following Algorithm 3. The data is presented in the dimensionless unit of $Q\tilde{d}$. In practical regression analysis, the initial guess for $\tilde{d}$ is determined as $\frac{2\pi}{\tilde{Q}}$, with $\tilde{Q}$ representing the position of the first correlation peak in $I(Q)$. Within the probed range of $Q\tilde{d}$, we observe quantitative agreement between the SANS experimental data and

Algorithm 3: Least squares curve fitting

Input: $I_{\mathrm{exp}}(Q\tilde{d})$, $f_{\mathrm{NN}}(Q\tilde{d}, \Xi)$, initial guesses Ξ^{i}, C^{i} and $I^{\mathrm{i}}_{\mathrm{inc}}$
Result: Ξ_{NN}

$\Xi \leftarrow \Xi^{\mathrm{i}}$
$C \leftarrow C^{\mathrm{i}}$
$I_{\mathrm{inc}} \leftarrow I^{\mathrm{i}}_{\mathrm{inc}}$; `// initial guess`
$i \leftarrow 0$
while $i <$ Maxiter **do**
  $I_{\mathrm{NN}}(Q\tilde{d}) \leftarrow f_{\mathrm{NN}}(Q\tilde{d}, \Xi)$; `// generate` $I_{\mathrm{NN}}(Q\tilde{d})$
  $I(Q) \leftarrow CI_{\mathrm{NN}}(Q\tilde{d}) + I_{\mathrm{inc}}$; `// generate` $I(Q)$
  $L_{\mathrm{fit}} \leftarrow \left\| I_{\mathrm{exp}}(Q\tilde{d}) - I(Q\tilde{d}) \right\|^2$; `// evaluate regression loss`
  Update Ξ, C, and I_{inc} with `L-BFGS-B` algorithm to minimize L_{fit}
  $i \leftarrow i + 1$
  if $L_{\mathrm{fit}} < L_c$ **then**
    $\Xi_{\mathrm{NN}} \leftarrow \Xi$; `// return the fitting result`
  end
end

the optimized $I(Q\tilde{d})$. Nevertheless, significant disparities become apparent for solutions with 30% and 40% AOT when $Q\tilde{d} \leq 1$. The explanation for this observation will be addressed in the subsequent section of this report. The discrepancy between the symbols and the dotted lines suggests that the widely used lamellar model [5] is inadequate for describing the structure of the lyotropic phases examined in this report.

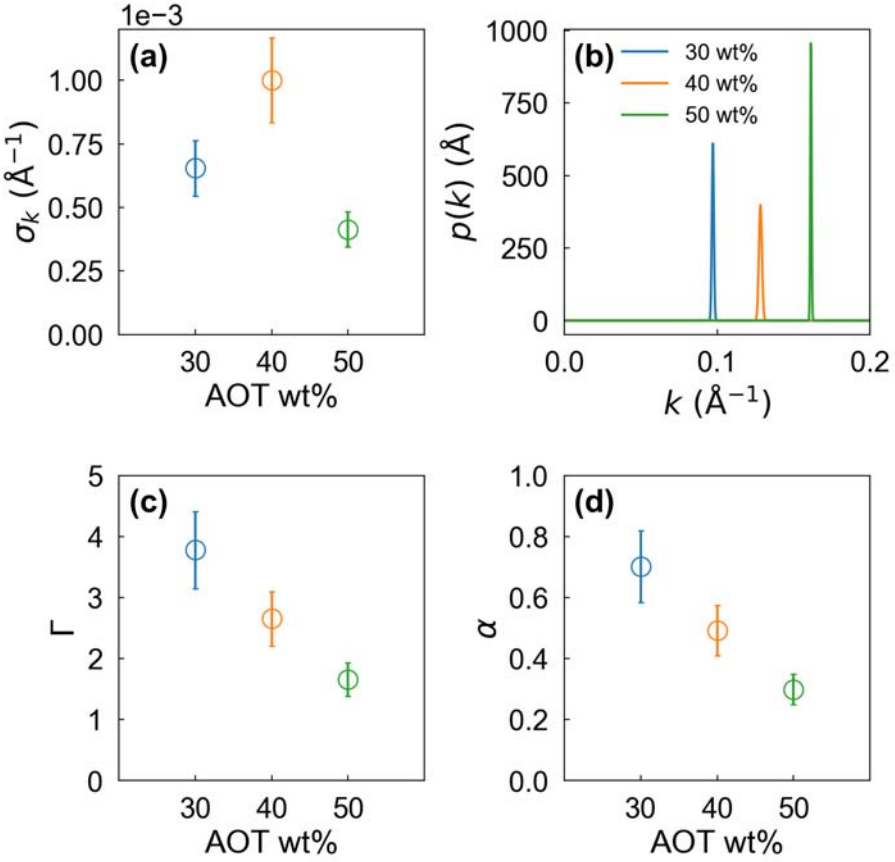

Figure 7: Values for (a) σ_k, (c) Γ, and (d) α in aqueous AOT solutions obtained via regression analysis of corresponding SANS data. Panel (b) presents the distribution of wave vector magnitude $f(k)$.

The relevant parameters determined from the regression of the scattering experiment are given in Fig. 7. Panels (a) and (b) present σ_k, and the corresponding distribution of wave vector magnitude $p(k)$ are given in extracted from regression. The findings support the conclusion that the standard de-

viation typically accounts for less than 5% of its mean. For the derivation of scattering cross sections in L_3 bicontinuous phases using the clipped random wave model—a mathematically refined extension of the LW model—a different spectral function is employed. This spectral function encompasses both the second and fourth moments of a Gaussian distribution [24, 25]. Given that the relevant values of wave vectors k are tightly clustered around their mean, we can reasonably conclude that a standard normal distribution adequately addresses density fluctuations in typical lyotropic structures.

Fig. 7 (c) illustrates the extracted orientational order parameter Γ. As the weight fraction of AOT increases, Γ decreases. This observation indicates that the distribution of wave vectors becomes progressively less anisotropic, suggesting a growing structural aspect of the L_3 sponge state within the L_α phases as the lamellar order deteriorates. Fig. 7 (d) illustrates the relationship between the extracted parameter α and the weight fraction of AOT. In the framework of the LW model, α serves as a quantitative indicator of anisometricity, specifically reflecting the relative composition of two immiscible phases. The observation of α decreasing from approximately 0.7 to around 0.3 as the AOT weight fraction increases from 30% to 50% is not surprising. This reduction in α reflects a decrease in the imbalanced ratio of water to AOT as the lyotropic system approaches isometric.

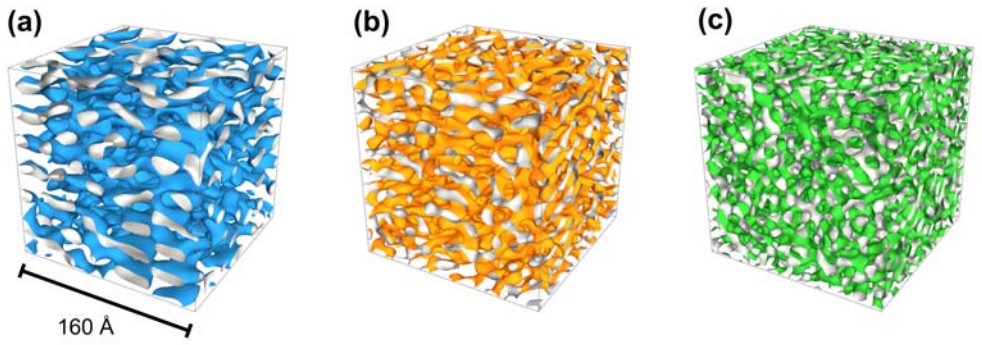

Figure 8: Three-dimensional visualizations of the lyotropic structures in aqueous AOT solutions at weight fractions of (a) 30%, (b) 40%, and (c) 50%.

Using the extracted values of σ_k, Γ, and α, as displayed in Fig. 7, a three-dimensional representation of lyotropic structures can be constructed by applying the GLW framework as shown in Fig. 8. Firstly, the inter-planar

spacing is on the order of several tens of Å. Secondly, as the AOT weight fraction increases, pathways between adjacent plates begin to develop gradually, resulting in a substantial increase in interconnections between layers. This transformation causes a shift in the arrangement of the initially anisotropic, two-dimensional plates at the mesoscopic length scale, transitioning them into a much more isotropic phase.

We can offer a quantitative account of this observed conformational progression by relying on the pertinent length scales as indicated in Fig. 9, which define the unique characteristics of the three analyzed stacked lamellar systems: Panel (a) presents the average inter-planar spacing, denoted as $d \equiv 2\pi\tilde{d}$. As the AOT weight fraction rises from 30% to 50%, this parameter decreases from about 60 Å to 40 Å. Panel (b) gives the in-planar spatial correlation length, denoted as $d_\perp$, based on the averaged spatial period of Moiré stripes [33]. This parameter signifies the shortest distance over which the normal vector of a lamellar plane maintains its alignment. Mathematically, $d_\perp$ is defined as

$$d_\perp \equiv \frac{d}{\sin\sigma_\theta}, \tag{5}$$

where σ_θ is the standard deviation of $P(\theta)$ given in Eqn. (2) and is defined as

$$\sigma_\theta \equiv [\frac{\int_0^\pi P(\theta)\theta^2 \sin\theta d\theta}{\int_0^\pi P(\theta)\sin\theta d\theta}]^{\frac{1}{2}}, \tag{6}$$

As the weight fraction of AOT is increased, the average value of $d_\perp$ decreases

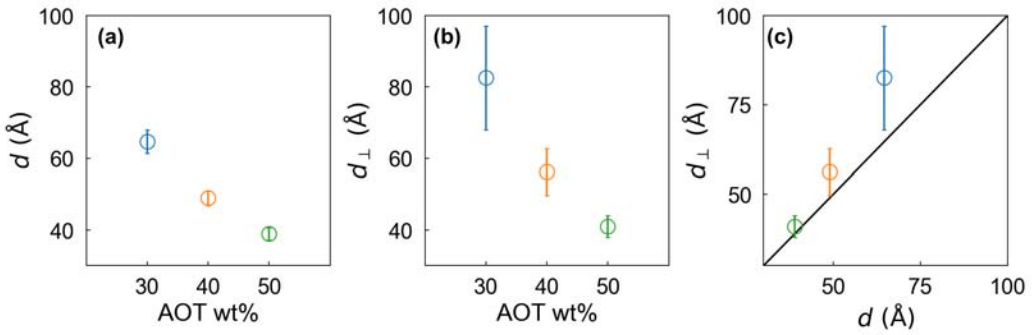

Figure 9: Two characteristic length scales of typical lyotropic phases are shown: (a) the mean inter-planar spacing denoted as d and (b) the in-planar spatial correlation length represented by $d_\perp$. The comparison between these lengths is presented in (c).

from 80 Å to 40 Å. This observation indicates that the individual plates

forming the stacked lamellar phases are progressively undergoing crumpling. In Fig. 9 (c), we compare the values of $d_\perp$ and d. The diminishing ratio of $\frac{d_\perp}{d}$ indicates that the wave vector field characterizing the lyotropic systems becomes more isotropic. This quantitative analysis aligns with the qualitative observation depicted in Fig. 8, indicating a gradual shift in conformation from a more lamellar-like arrangement to a more sponge-like configuration.

Vital insights into the local topological characteristics can be directly derived from the three-dimensional structures of lyotropic phases in real space, as illustrated in Fig. 8. Before discussing the extracted information given in Fig. 10, we briefly introduce surface curvatures: The inherent topological characteristics of two-dimensional surfaces can be thoroughly examined by delving into their morphology according to differential geometry [34]. Let's assume that the surfaces depicted in Fig. 8 can be represented by a function $F(x, y, z) = 0$. In this context, the normal vector field, denoted as $\hat{U}$, is defined as $\hat{U} \equiv \frac{\nabla F}{|\nabla F|}$. For any given point p residing on one of these surfaces, we can establish a shape operator S_p by considering the directional gradient along the tangent vector $\vec{v}$ at p. It can be expressed as $S_p(\vec{v}) \equiv -\nabla_v \hat{U}$. Geometrically, $S_p(\vec{v})$ represents the surface curvature in the vicinity of p. The magnitude of $S_p(\vec{v})$ corresponds to the reciprocal of the radius of an osculating circle on the surface that is perpendicular to the plane formed by $\hat{U}$ and $\vec{v}$.

Since $S_p(\vec{v})$ is a symmetric matrix, it can be diagonalized. The two resulting eigenvalues, denoted as $\frac{1}{R_1}$ and $\frac{1}{R_2}$, are known as the principal curvatures. These values represent the maximum and minimum values of the normal curvature at p, where the normal curvature $\frac{1}{R}$ is calculated as $-\nabla_u \hat{U} \cdot \vec{u}$, with $\vec{u}$ being the unit tangent vector at p. From $S_p(\vec{v})$ and its eigenvalues, we can define two fundamental invariants: the Gaussian curvature K and the mean curvature H. Specifically, the Gaussian curvature is expressed as $K \equiv \frac{1}{R_1 R_2}$, and the mean curvature as $H \equiv \frac{1}{2}\left(\frac{1}{R_1} + \frac{1}{R_2}\right)$. These quantities correspond to the determinant and half the trace of the shape operator $S_p(\vec{v})$, respectively.

Fig. 10 presents the probability distribution functions for H and K, referred as $p(H)$ and $p(K)$ respectively. These distributions are computed from the three-dimensional structures of lyotropic phases displayed in Fig. 8. The probability distribution $p(H)$ shown in Fig. 10 (a) exhibits a noticeable left-skew. Furthermore, as the weight fraction of AOT increases, the distribution of $p(H)$ becomes broader. Considering the definition of H, it becomes ev-

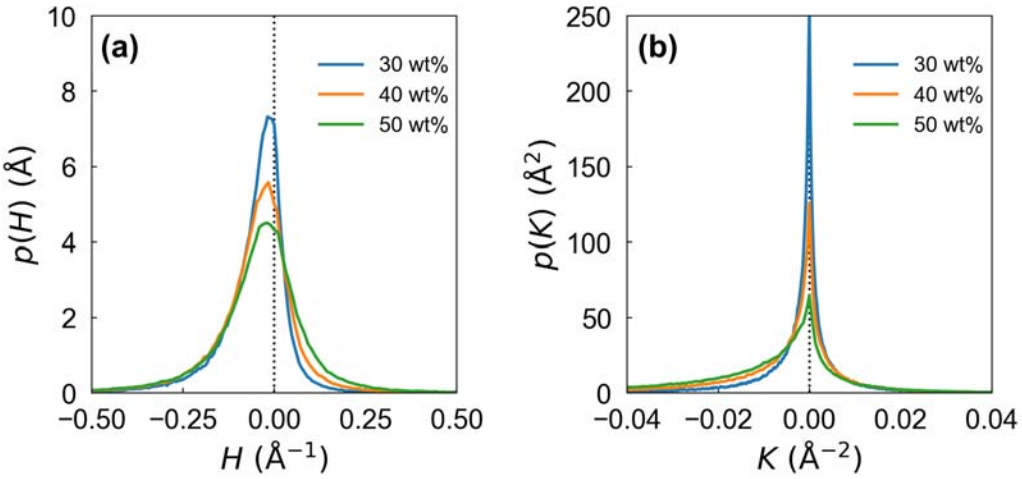

Figure 10: Probability distribution functions for (a) mean curvature (H) and (b) Gaussian curvature (K) in aqueous AOT solutions.

ident that in solutions with lower AOT weight fractions, a greater number of the local wrinkling on the crumbled surfaces exhibit an outward curvature, thereby giving rise to a convex shape extending towards the water-rich region.

Much like the distribution of $p(H)$ described in Fig. 10 (a), the distributions of $p(K)$ also display left-skew tendencies, particularly showing increased variance as the AOT weight fraction increases (Fig. 10 (b)). By considering the definition of K, it becomes apparent that surfaces in solutions with higher AOT weight fractions exhibit more pronounced wrinkling, as the broader distribution implies smaller values for the corresponding R_1 and R_2.

We emphasize that considerable attention is directed towards establishing a comprehensive framework for describing the thermodynamic characteristics of general lyotropic systems [19, 20]. In this endeavor, Helfrich pioneered by formulating the Hamiltonian for lipid bilayers in relation to mean and Gaussian curvatures, alongside their associated moduli [35]. In the context of elucidating phase transitions in lyotropic phases, it is imperative to obtain measurements of mean and Gaussian curvatures as integral components. These measurements, therefore, constitute a fundamental facet of experimental investigations. In this regard, the efficacy of our proposed method in providing these statistically averaged topological characteristics of lyotropic phases from scattering techniques has been validated.

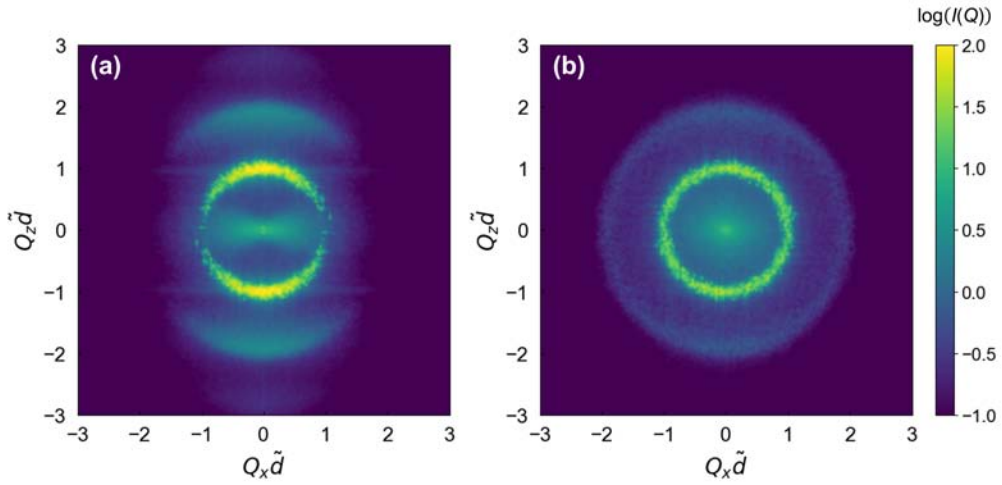

Figure 11: (a) A 2D scattering spectrum of a single domain with vertically stacked lamellar planes, where the average normal vector aligns perpendicular to the incident particle beam along the y-axis. (b) The scattering spectrum was obtained from a polygrain sample comprising stacked lamellar plates, with each individual grain's local topology resembling that of the single grain displayed in Panel (a).

Investigating the underlying reasons for the evident disparity between experimental SANS data and the best-fit curve generated by the CNN regression framework in the low Q region of $Q\tilde{d} \leq 1$, as depicted in Fig. 6, is of considerable importance. Fig. 11 displays the two-dimensional coherent scattering intensities of a lyotropic structure composed of crumbled lamellar planes generated by the GLW. Panel (a) presents the spectrum originating from a single domain of vertically stacked lamellar planes, where the average normal vector is oriented perpendicular to the direction of incident particles. Due to the prevalent alignment of these stacked planes, the resulting spectrum exhibits anisotropic characteristics. Panel (b) displays the scattering spectrum acquired from a sample containing polygrains made up of stacked lamellar plates. The local topology of each individual grain is statistically equivalent to that of the single grain depicted in Panel (a). In this case, the normal vector of each grain is randomly oriented, and the angular averaging process is appropriately applied in the spectrum calculation, as in our training process. Consequently, the resulting spectrum exhibits angular isotropy.

A visual examination of Fig. 11 (a) shows that in the range of $Q\tilde{d} \leq 1$, the coherent scattering intensity is significantly greater along the $Q_x\tilde{d}$ direction compared to the $Q_z\tilde{d}$ direction. In the case of a lyotropic system characterized by the L_α phase, the process of loading the sample may inadvertently lead to a non-uniform distribution of orientation among the normal vectors of individual constituent grains, potentially resulting in a modification of the coherent scattering at low values of Q. Conversely, in the case of a lyotropic system exhibiting the L_3 topological nature, the sample loading process will have no impact since the system is inherently isotropic. This argument clarifies why the discrepancy is most evident in the case of a 30% AOT solution, which exhibits the most prominent lamellar order, becomes notably less pronounced in a 40% AOT solution, and virtually vanishes in a 50% AOT solution displaying a pronounced sponge-like topological character.

Hence, we contend that the low-Q coherent scattering data, as depicted in Fig. 6, may not necessarily depict the equilibrium structure of the lyotropic systems examined in this report. To thoroughly capture the hierarchical structural characteristics encompassing both macro and mesoscopic length scales, an approach that complements the CNN regression analysis in this report is to conduct a two-dimensional spectral analysis using data collected from different projection planes with varying rotation or tilt angles with respect to the incident particle beam. This inversion method can be aided by orthogonal decomposition schemes such as the real spherical harmonic expansion [36]. Nevertheless, a comprehensive implementation of this method falls beyond the scope of this report.

4. Concluding Discussion

We have introduced an innovative deep learning inversion framework rooted in the principles of convolutional neural networks, designed for the precise extraction of morphological features in general lyotropic phases based on their scattering cross sections. This framework is underpinned by the foundational mathematical construct of generalized levelled waves. Within this framework, we employ the plane wave superposition method to assess density fluctuations in diverse lyotropic phases. As a versatile framework for delineating lyotropic topology, this mathematical approach integrates a regulated wave vector distribution to effectively account for the diverse degrees of anisotropy in density fluctuations present in lyotropic phases with distinct morphological characteristics. After performing computational benchmark-

ing to assess its numerical accuracy, the feasibility of this inversion framework is additionally affirmed through a SANS experimental examination of smectically stacked bilayers exhibiting different levels of lamellar order. Furthermore, the current dynamical investigations of lamellar phases primarily revolve around the structural framework of a one-dimensional lamellar model [11]. An area that warrants further exploration is the examination of how inter-planar passages affect the dynamic characteristics of distorted lamellar phases, utilizing the generalized leveled wave model introduced in this research.

Due to the broad applicability of the generalized levelled wave description framework, this methodology readily extends its utility to investigate the structural characteristics of a wide spectrum of lyotropic phases. This expanded approach is not confined solely to the non-particulate L_3 or L_α phases; rather, it encompasses crystalline phases like the hexagonal (H), cubic (Cub), and cholesteric (Ch) phases, which are frequently encountered in diverse applications, including biological membranes, detergents, and liquid crystal displays.

This research also underscores a promising avenue for future investigation: There is substantial interest in understanding the morphological transformations in flowing lyotropic phases under different deformation conditions, as evident from the distinct evolution of measured scattering cross-sections. Through appropriate consideration of the angular average of grain orientation, our methodology for analyzing one-dimensional scattering spectra can be seamlessly extended to a regression framework for the examination of two-dimensional anisotropic spectra. By accessing pertinent projection planes, we can quantitatively map out the flow-induced morphological changes with the assistance of eigen-decomposition methods, such as real spherical harmonic expansion.

Future investigations into these systems can expand upon the conceptual framework of generalized levelled wave model introduced in this report. Within the realm of lyotropic research, a compelling area of interest centers on the persistent fascination with the lamellar-to-isotropic transition. This transition is a crucial element in understanding the phase characteristics of microemulsions, marked by the emergence of perforations that facilitate the merging of initially isolated bilayer membranes into a continuous interconnected domain. In the mathematical context of generalized leveled waves, these topological irregularities can be clearly discerned through curvature analysis. It is foreseeable that a significant increase in defect density will

occur as anisotropy diminishes, and surfaces adopt a progressively twisted configuration. With the ability to discern topological defects, it may be possible to establish an order parameter rooted in defect density for tracking phase transitions within this significant category of soft matter.

5. Acknowledgement

We gratefully acknowledge Marianne Imperor and William A. Hamilton for their fruitful discussions and interest, which have significantly enhanced this work. This research was performed at the Spallation Neutron Source and the Center for Nanophase Materials Sciences, which are DOE Office of Science User Facilities operated by Oak Ridge National Laboratory. Molecular dynamics simulations used resources of the Oak Ridge Leadership Computing Facility, which is supported by DOE Office of Science under Contract DE-AC05-00OR22725. Application of machine learning to soft matter was supported by the U.S. Department of Energy, Office of Science, Office of Basic Energy Sciences Data, Artificial Intelligence and Machine Learning at DOE Scientific User Facilities Program under Award Number 34532. G.R.H. is supported by the National Science and Technology Council (NSTC) in Taiwan with Grant No. NSTC 111-2112-M-110-021-MY3. M.-C.C. thanks the support provided by the University at Albany - SUNY. YS is supported by the U.S. Department of Energy, Office of Science, Office of Basic Energy Sciences, Materials Science and Engineering Division. YW acknowledges the support by the U.S. Department of Energy, Office of Science, Office of Basic Energy Sciences, Early Career Research Program Award KC0402010, under Contract DE-AC05-00OR22725.

References

[1] Z. Zheng, R. Grünker, X. Feng, Synthetic two-dimensional materials: A new paradigm of membranes for ultimate separation, Adv.Mater. 28 (2016) 6529–6545.

[2] S. P. Nunes, P. Z. Culfaz-Emecen, G. Z. Ramon, T. Visser, G. H. Koops, W. Jin, M. Ulbricht, Thinking the future of membranes: Perspectives for advanced and new membrane materials and manufacturing processes, J. Membr. Sci. 598 (2020) 117761.

[3] S. Prévost, M. Gradzielski, Th. Zemb., Self-assembly, phase behaviour and structural behaviour as observed by scattering for classical and non-classical microemulsions, Adv. Colloid Interface Sci. 247 (2017) 374–396.

[4] G. Porte, Chapter 12. Surfactant micelles and bilayers: Shapes and interactions, in: Neutron, X-Ray and Light: Scattering Methods Applied to Soft Condensed Matter, edited by Th. Zemb and P. Lindner, North-Holland, Amsterdam, 2002, pp. 299–315.

[5] F. Nallet, R. Laversanne, D. Roux, Modelling x-ray or neutron scattering spectra of lyotropic lamellar phases : interplay between form and structure factors, J. Phys. II France 3 (1993) 487–502.

[6] C. G. Vonk, The small-angle scattering of distorted lamellar structures, J. Appl. Crystallogr. 11 (1978) 541–546.

[7] R. Zhang, R. M. Suter, J. F. Nagle, Theory of the structure factor of lipid bilayers, Phys. Rev. E 50 (1994) 5047–5060.

[8] J. Lemmich, K. Mortensen, J. H. Ipsen, T. Hønger, R. Bauer, O. G. Mouritsen, Small-angle neutron scattering from multilamellar lipid bilayers: Theory, model, and experiment, Phys. Rev. E 53 (1996) 5169–5180.

[9] G. Pabst, M. Rappolt, H. Amenitsch, P. Laggner, Structural information from multilamellar liposomes at full hydration: Full q-range fitting with high quality x-ray data, Phys. Rev. E 62 (2000) 4000–4009.

[10] G. Bouglet, C. Ligoure, Polymer-mediated interactions of fluid membranes in a lyotropic lamellar phase: a small angle x-ray and neutron scattering study, Eur. Phys. J. B 9 (1999) 137–147.

[11] M. Mihailescu, M. Monkenbusch, J. Allgaier, H. Frielinghaus, D. Richter, Neutron scattering study on the structure and dynamics of oriented lamellar phase microemulsions, Phys. Rev. E 66 (2002) 041504.

[12] F. Castro-Roman, L. Porcar, G. Porte, C. Ligoure, Quantitative analysis of lyotropic lamellar phases sans patterns in powder oriented samples, Eur. Phys. J. E 18 (2005) 259–272.

[13] G. Pabst, R. Koschuch, B. Pozo-Navas, M. Rappolt, K. Lohner, P. Laggner, Structural analysis of weakly ordered membrane stacks, J. Appl. Crystallogr. 36 (2004) 1378–1388.

[14] P. T. Callaghan, O. Soderman, Examination of the lamellar phase of aerosol OT/water using pulsed field gradient nuclear magnetic resonance, J. Phys. Chem. 77 (1983) 1737–1744.

[15] G. Chidichimo, C. La Mesa, G. A. Ranieri, , M. Terenzi, NMR investigation of the lamellar mesophase occurring in the system aerosol OT-water, Mol. Cryst. Liq. Cryst. 150b (1987) 221–236.

[16] L. Coppola, R. Muzzalupo, G. A. Ranieri, M. Terenzi, Characterization of the lamellar phase aerosol OT/water system by NMR diffusion measurements, Langmuir 11 (1995) 1116–1121.

[17] L. Coppola, R. Gianferri, I. Nicotera, C. Oliviero, A defective lamellar phase in a nonionic surfactant water system studied by NMR methods, Mol. Cryst. Liq. Cryst. 398 (2003) 157–167.

[18] G. Porte, Lamellar phases and disordered phases of fluid bilayer membranes, J. Phys.: Condens. Matter 4 (1992) 8649–8670.

[19] S. A. Safran, Statistical Thermodynamics of Surfaces, Interfaces, and Membranes, Addison-Wesley Publishing Company, Reading, 1994.

[20] D. Nelson, S. Weinberg, T. Piran, Statistical Mechanics of Membranes and Surfaces, 2nd Ed., World Scientific Publishing Company, New Jersey, 2004.

[21] I. W. Hamley, Diffuse scattering from lamellar structures, J. Appl. Crystallogr. 18 (2022) 711–721.

[22] N. F. Berk, Scattering properties of a model bicontinuous structure with a well defined length scale, Phys. Rev. Lett. 58 (1987) 2718–2721.

[23] N. F. Berk, Scattering properties of the leveled-wave model of random morphologies, Phys. Rev. A 44 (1991) 5069–5079.

[24] D. Choy, S.-H. Chen, Clipped random wave analysis of isometric lamellar microemulsions, Phys. Rev. E 61 (2000) 4148–4155.

[25] D. Choy, S.-H. Chen, Clipped random wave analysis of anisometric lamellar microemulsions, Phys. Rev. E 63 (2001) 021401.

[26] Th. Zemb, Chapter 13. Scattering by microemulsions, in: Neutron, X-Ray and Light: Scattering Methods Applied to Soft Condensed Matter, edited by Th. Zemb and P. Lindner, North-Holland, Amsterdam, 2002, pp. 317–350.

[27] R. A. Fisher, Dispersion on a sphere, Proc. Math. Phys. Eng. Sci. 217 (1953) 295–305.

[28] C. Do, H.-S. Jang, S. R. Kline, S.-M. Choi, Subdomain structures of lamellar and reverse hexagonal pluronic ternary systems investigated by small angle neutron scattering, Macromolecules 42 (2009) 2645–2650.

[29] G. Strang, Introduction to Linear Algebra, 5th Ed., Wellesley-Cambridge Press, Wellesley, 2016.

[30] J. Rogers, P. A. Winsor, Change in the optic sign of the lamellar phase (G) in the aerosol OT/water system with composition or temperature, J. Colloid Interface Sci 30 (1969) 247–257.

[31] P. G. Petrov, S. V. Ahir, E. M. Terentjev, Rheology at the phase transition boundary: 1. lamellar L_α phase of AOT surfactant solution, Langmuir 18 (2002) 9133–9139.

[32] G.-R. Huang, C.-H. Tung, M.-Z. Chen, L. Porcar, Y. Shinohara, C. Wildgruber, C. U. Do, , W.-R. Chen, Desmearing small-angle scattering data by central moment expansions, J. Appl. Cryst. 56 (2023) 1537–1543.

[33] E. Goodwin, J. Wyant, Field Guide to Interferometric Optical Testing, Field Guides, SPIE, 2006.

[34] E. Kreyszig, Differential Geometry, University of Toronto Press, Toronto, 1964.

[35] W. Helfrich, Elastic properties of lipid bilayers: Theory and possible experiments, Z. Naturforsch. 28 (1973) 693–703.

[36] G.-R. Huang, Y. Wang, B. Wu, Z. Wang, C. Do, G. S. Smith, W. Bras, L. Porcar, P. Falus, W.-R. Chen, Reconstruction of three-dimensional anisotropic structure from small-angle scattering experiments, Phys. Rev. E 96 (2017) 022612.